Lanthanide luminescence to mimic molecular logic and computing through physical inputs

M.A. Hernández-Rodríguez[1]

[1] Physics Department, IMN, IUdEA and MALTA Consolider Team, La Laguna University, Apdo. 456, E-38200 San Cristóbal de La Laguna, Santa Cruz de Tenerife, Spain

Carlos D. S. Brites,[2] Luís D. Carlos[2]

[2] Physics Department and CICECO-Aveiro Institute of Materials, University of Aveiro, 3810-193 Aveiro, Portugal.

G. Antorrena[3]

[3] Laboratorio de Microscopías Avanzadas (LMA), Instituto de Nanociencia de Aragón (INA), Universidad de Zaragoza, Edificio I+D, C./Mariano Esquillor s/n., 50018 Zaragoza (Spain)

Rafael Piñol,[4] Angel Millan,[4] R. Cases[4]

[4] Departamento de Física de la Materia Condensada, Facultad de Ciencias and Instituto de Ciencia de Materiales de Aragón, CSIC–Universidad de Zaragoza, 50009 Zaragoza (Spain)

M Rodrigues,[5] L. Pérez-García[5]

[5] Department de Farmacologia i Química Terapèutica and Institut de Nanociència i Nanotecnologia UB (IN2UB), Universitat de Barcelona, Avda. Joan XXIII s/n, 08028 Barcelona (Spain)

N. Torras,[6] J. A. Plaza[6]

[6] Instituto de Microelectrónica de Barcelona, IMB-CNM (CSIC), Campus UAB, 08193 Bellaterra, Barcelona (Spain)

I. Díez[7]

[7] Department of Applied Physics, Aalto University Helsinki, Finland

E-mail:

1. Introduction

During these last decades, the technology of the information has been growing up considerably, since the first digital-programmable computer was developed[1]. Computers and related systems have become more efficient and smaller because of the scaling shrinkage of the silicon-based components over a relatively short period of time. Nevertheless, there is a general interest to become computers even smarter and powerful and the only way to achieve such purpose, is designing a miniaturised scale of the computer circuit components[2]. Classical miniaturisation of computer with silicon-based components, eventually is reaching it limits, in terms of physical limitations[3] and high economical costs[4]. In this sense, it is when molecular logic gates come into consideration, allowing the integration of self-assembly molecular technology whose dimensions are in the order of atom sizes[5]. From their discovery in 1993 by Silva et.al.[6], some many other works regarding molecular logic gates and some applications developed by the same group have been published[7–11].

Molecular logic gates allow the implementation of biological entities, for instance, supramolecules, organic molecules, proteins, DNA and even polymers used as input signals to mimic the logical functions of a certain semiconductor-based electronic device[12–16]. The output signal is the fluorescence light, whose detection does not need any contact with the probe, which is interesting from the point of view of sensing and detection. In recent years, increasing attention has been paid to the development of molecular logic gates based on that converts chemical information (anions and/or cations detection) into fluorescent signals[13,17,18]. For example, a naphthalene-quinoline based chemical sensor in which fluorescence and absorbance-ratiometric as optical outputs were used for the Al^{3+} detection,[19] responsible of some diseases in humans, when its presence is abundant. As this example, some other works focused on this have been reported in recent years.

Interesting are, and relatively recent, those molecular logic gates in which the optical outputs come from lanthanide luminescence. The use of lanthanide ions as luminescent reporters in such devices is particularly attractive as ions such as Eu^{3+}, Tb^{3+}, Nd^{3+} or Yb^{3+} emit at long wavelengths, with characteristic line-like emission bands and long-lived excited state lifetimes, also employed in luminescent sensing, overcoming the autofluorescence and light dispersion from biological media[20–28].

More recently, lanthanide metalorganic frameworks (LnMOFs) have attracted considerably the attention for chemical detection due to the combination of intrinsic

luminescence features and intrinsic porosity of MOFs. In addition, chemical sensors based on LnMOFs have been widely researched for the detection of metal anions and cations, temperatures, pH values and even small molecules[29–34]. Due to these sensing capabilities, the application of such materials as molecular logic gates have been studied and reported by Xu et al.[35] in whose work, fluorescence material- Eu^{3+}@UMOFs has been developed for effective combination of ions (Hg^{2+}, Ag+, and S^{2-}) detection and logic computing, leading to a molecular logic gate, particularly useful in environmental monitoring due to the nature of the chemical inputs.

More interesting and less explored are those molecular logic gates that involves physical inputs, reported by M. Rodrigues et al.[36]. Such work, the authors show the application of a Eu^{3+}-Tb^{3+} based -self-assembled polymer monolayer functionalized Si surface (SAM) as an optically active molecular demultiplexer, whose both inputs (excitation wavelength and temperature) and outputs (ratiometric thermometric parameters of two different regimes, due to the bistability behaviour with the temperature of this system) are physical, being the first one reported in the literature.

2. Results and discussion

Monocrystalline silicon wafers were used as substrates for thermometric SAM deposition as previously described[AFM] In a first step a layer of SiO_2 was deposited by plasma-enhanced chemical vapor deposition (PECVD). The SiO2 surface is activated by treatment with UV/ozone to generate –OH groups and amine modified with APTES by vapor deposition at low pressure. Then, acetoacetyl polyethylenglycol acrylate (acacPEGA) polymer chains are attached to the amine-modified surface by a Michael addition of the acrylate groups onto the surface amine. Finally, thermometric luminescence probes consisting on Eu^{3+} and Tb^{3+} lanthanide complexes are anchored to the surface by quelation of $Ln^{3+}(DPA)_2$ molecules with the keto-ester acac terminal groups. The length of the PEG polymer spacer was varied from 100 to 3000 kD.

2.1 Temperature dependent luminescence

The self-assembled monolayer (SAM) of polymer functionalized Si surface doped with Tb^{3+}-Eu^{3+} with the longest organic chain to the shortest one (Z6D1, Z3D1 and Z1D1, respectively) were selected to perform the ratiometric characterization.

The excitation spectra at ambient conditions of the Z6D1 sample, monitoring the $^5D_4 \rightarrow {}^7F_5$ (Tb^{3+}) and the $^5D_0 \rightarrow {}^7F_2$ (Eu^{3+}) transitions respectively, are shown in **Figure 3a**. An intense broad band is observed in both spectra (250-290 nm), mostly associated to the

DPA ligand excited single states [23,37]. Since both excitation spectra are similar and no intra $4f^8$ transitions lines were observed, then it can be neglected the energy transfer from of Tb^{3+}-to-Eu^{3+} and the deactivation channels are mainly regulated by the ligand.

The emission spectra in a single heating-cooling cycle from 295 K up to 369 K exciting at 271.5 nm of Z6D1 sample are shown in **Figure 3b**. As the temperature increases, the integrated emission areas associated to the $^5D_4 \rightarrow {}^7F_5$ (Tb^{3+}) and $^5D_0 \rightarrow {}^7F_2$ (Eu^{3+}) transitions decrease (see **Figure 3c**). However, this decrease rate of the integrated emission areas is not homogeneous in the sense that the relative intensity decrease is notably higher in the emission band associated to the $^5D_4 \rightarrow {}^7F_4$ (indexed as I_1) transition compared to the one related to the $^5D_0 \rightarrow {}^7F_2$ transition (identified as I_2). Another aspect to mention from the temperature evolution of emission spectra, is that during the cooling process the resolution of the emission bands associated to the $^5D_0 \rightarrow {}^7F_2$ (Eu^{3+}) and $^5D_4 \rightarrow {}^7F_4$ (Tb^{3+}) transitions are clearly higher than the ones during the heating ramp, suggesting a possible distortion of the local symmetry (lower symmetry configuration during cooling process in the sample) of the ions environment, leading to the total breakdown of the degeneracy of the $^{2S+1}L_J$ multiplets of the free Eu^{3+} and Tb^{3+} ions, resulting in 2J+1 Stark levels. This behaviour with temperature can be also observed in samples with larger organic changes, i.e. Z3D1 and Z1D1 (for simplicity, not shown here). The energy of the triple state of the DPA ligand is around of 27050 cm^{-1} [38,39], preventing the $^5D_4$ -to-ligand and $^5D_0$-to ligand energy back-transfer which is the main responsible of the luminescence quenching, as often happens in other Tb^{3+} /Eu^{3+}-based molecular optical temperature sensors[40].

Probably the most interesting feature of the temperature dependent luminescence, is that it depends on the temperature change induced in the surface. Heating up from 295 K to 369 K, the I_1 and I_2 integrated areas decrease 70% and 30%, respectively, relatively to the values at 295 K. During the cooling stage, the values of the intensities are not recovered at all compared to the initial values[41], showing a clearly hysteretic behaviour with temperature.

The relationship between I_1 and I_2 can be used as a ratiometric thermometric parameter in order to know the surface temperature of the SAM samples, during the heating and/or cooling stages. Such parameter is defined as $\Delta = I_1/I_2$. The temperature evolution of this parameter in a single heating-cooling cycle for three SAM samples with different organic chain lengths, from the longest one (Z1D1) to shortest one (Z6D1) is shown in **Figure 4**.

From this figure, it is clear that the implementation of the lanthanide complex thermometric system on this type of SAM leads to a very different behaviour in the thermometric process compared to other Eu^{3+}/Tb^{3+}-based thermometric systems, [38,40,42,43], because such behaviour is related to thermal induced change in the surface, being a recurrent trend in all samples. During the heating stage from 295 K up to 369 K, Δ in all samples shows a linear decrease with temperature, probably due to the activation of nonradiative decay pathways involving the acacPEGA organic chains, depopulating the $^5D_4$ and $^5D_0$ emitting levels respectively. However, during the cooling ramp a double behaviour in Δ can be observed, and the temperature in which this happens is practically the same for all samples (around 313 K), indicating that this behaviour does not depend on the organic chain length, and the presence of this double behaviour with temperature confirms the bistability of these samples.

Regarding systems showing bistability behaviour, many examples of luminescent lanthanide-based materials can be found in the literature with such behaviour[44,45], and some cases it can be related to higher power densities used plus the energy transfer processes that can happen between lanthanide ions, such as back transfer from Yb^{3+} to Nd^{3+} ions in $NdPO_4$ matrix [46]. Nevertheless, the samples of the present work were excited using very low power densities, so the thermal gradients induced within the samples were negligible. In addition, as it mentioned above there is no evidence of energy transfer from Tb^{3+} to Eu^{3+} ions and, thus the bistability can be directly associated to structural changes in the acacPEGA organic chains.

Linear equations were well fitted to the experimental data of Δ. From the fitting process, the relative sensitivity (S_{REL}) was estimated for each sample and for both heating and cooling stages according to the equation:

$$S_r = \frac{1}{\Delta}\left|\frac{\partial \Delta}{\partial T}\right| \qquad (1)$$

During the heating process it is clear to see that the S_{REL} not only depends on the temperature (increases as the temperature increases) but also on the organic chain length, being the maximum values of S_{REL} at 369 K, (**Figure 4b**) 2.84% K^{-1}, (**Figure 4d**) 2.73% K^{-1} and (**Figure 4f**) 2.27% K^{-1} with temperature uncertainties, δT, around of 0.1-0.3 K (**Figure 5**) from the longest to the shortest organic chain length, respectively, calculated according to the following equation:

$$\delta T = \frac{1}{S_r} \frac{\delta \Delta}{\Delta} \qquad\qquad (2)$$

These thermal S_{REL} are very high compared to others Ln-based optical sensors (see **Table 1**), suggesting the application of such materials as optical sensors working at high temperatures and even within the physiological range of temperatures (303 K – 320 K). Concerning the cooling process, the samples show very low S_{REL} in the range between 369 K to 313 K (regime 1), while in the range from 313 K to 296 K (regime 2), S_{REL} are incredible high, whose maximum values are 4.75 % K^{-1}, 4.5% K^{-1} and 2.6% K^{-1} for Z1D1, Z3D1 and Z6D1 respectively. However, these S_{REL} during the cooling process are time-dependant due to the bistability, especially in regime 2 because the organic chains trend to recover their original configuration in long time periods[41].

2.2 Surface structure characterization

2.2.1 XPS Characterization

Samples were analysed in two different steps of the fabrication process, before and after the formation of the lanthanide complex.

XPS surfaces after reaction with acacPEGA (figure 1) show C 1s region that can be fitted into four main peaks, at 285.0 eV (C-C, calibration), +1.7(1) eV, +3.2(1) eV and +4.2(1) eV that correspond to the four oxidation states of C in acacPEGA structure (C-C, C-O, O-C-O / C=O and O-C=O respectively) C-C peak has been fitted using two peaks in some samples in order to mathematically optimize the fitting (It could be explained due to effect of second order neighbours).

There is a remarkable difference in the intensity of C-O peak depending on the length of the organic chain. It should be expected a continuous decrease of C-O signal with the shortening of the organic chain. However the maximum of C-O signal does not occur in Z1A and Z1C but in Z3A and Z3C1. C-O represents about 50% of C 1s signal in Z3A / Z3C and about 30% in Z1A/Z1C and Z6A/Z6C which suggest that the functionalization process is less effective in case of long organic chains. These results are reproduced using a bigger series of different organic chain lengths (supporting info? Z1B, Z1B, Z1B, Z1B, Z1B and Z1B). The result is also corroborated by a lower concentration of Eu and Tb after the anchoring process of the lanthanide complexes in case of larger organic chains (Supporting info)

The incorporation of lanthanides (Eu and Tb) into the coating was also confirmed by XPS that showed the presence of both elements after the anchoring process of the lanthanide ß-keroester complexes (Figure 2). Eu 3d and Tb 3d are the most intense core levels in photoemission spectra. The oxidation state of Eu and Tb in these systems has been discussed before.[36] It is not possible to unequivocally determine the oxidation state of this elements from the XPS experiment but it is worth to notice the different behaviour observed depending on the length of the organic chain (Figure 2 Insert). Eu 3d presents the expected spin orbit splitting $3d_{5/2}$ and $3d_{3/2}$. Eu $3d_{5/2}$ region presents two main peaks at about 1225 eV and 1235 eV and Eu $3d_{3/2}$ at about 1255 and 1265 eV. The peaks at about 1225eV ($3d_{5/2}$) and 1255 eV ($3d_{3/2}$) are assigned to Eu^{2+} and the ones at 1235 eV ($3d_{5/2}$) and 1265 eV($3d_{3/2}$) to Eu^{3+}. However it is also reported that Eu^{2+} may present shake up signals at the expected position of Eu^{3+} and the reverse for shake down process of Eu^{3+}. In any case it is observed that the ratio of mixed valence state or the shake up/down processes are affected by the organic chain length.

Spectra of series B and D, fabricated using 48h instead of 24h reaction times between polymer and surface amines, respectively, are equivalent indicating that this factor has little influence in the structure of the coating.

2.2.2. FESEM and AFM Characterization

FESEM analysis of thermometric surfaces (Fig. S1) shows a very smooth surface and a uniform chemical composition in those samples with medium and small spacer PEG polymer length, whereas that of the sample with the longest polymer length shows some degree of granulation and chemical heterogeneity.

AFM analysis (Fig. S2) shows a clear increase of the surface roughness on the thermometric functionalized samples with respect to amine-modified samples. However, it does not show any change on the surface topography when the temperature is increased from RT to 60 $^{\circ}$C (Figs. S3-5).

2.2 Molecular logic gate

Due to the bistability behaviour of these samples with temperature, their possible application as molecular logic gate is discussed in this section. As it is known, molecular logic gates, the molecules mimic the well-known logical functions of a certain semiconductor-based electronic device. Unlike, the classical electronic devices, molecular logic gates allow the implementation of biological entities, for example, cells. The output signal is the fluorescence light, whose detection does not need any contact

with the probe. Many works focused on this issue have been reported, for instance logic gates that convert chemical information into fluorescent signals which have attracted much attention in recent years [18–22]. More interesting and less explored are those molecular logic gates that involves physical inputs, such as the excitation wavelength and temperature [36].

The Tb^{3+} / Eu^{3+} -based SAM studied in this work can be employed for the construction of optically active molecular logic gates, with both physical inputs and outputs. In this sense, the three inputs of these molecular logic gates are the excitation wavelength (λ_{EXC}), the temperature (T) whose value can be lower or higher than the temperature at which the regime change occurs in the cooling phase (Tc = 313 K) and finally, the thermal gradient (ΔT) that will indicate whether the samples are being heated or cooled from 295 K up to 369 K in heating-cooling cycles. While the outputs are the relative sensitivities during the heating regime (S_{REL}^{A}) and the two ones associated with cooling (S_{REL}^{B} and S_{REL}^{C}, when T>Tc and T<Tc respectively) regimes.

When the input associated to λ_{EXC} takes the value 0, there is no emission and therefore the outputs take the value 0. When the physical input of the excitation takes the value 1, and the rest of the physical inputs take the value 0, then the S_{REL}^{C} output takes the value 1, which would be the relative sensitivity associated with regime 2 of the cooling stage. If under the same conditions, the physical input T takes the value 1 (T>Tc), then the output S_{REL}^{B} is 1, being the value of the relative sensitivity in the cooling regime 1. As soon as the inputs ΔT and T take the value 1 (heating) and 0 (T<Tc) respectively, then the S_{REL}^{A} output takes the value 1, representing the values of the sensitivity during the heating stage at temperatures below Tc. The last case would be both ΔT and T taking the value 1 (heating and T>Tc) then, S_{REL}^{A} takes the value 1, being the values of the relative sensitivity during the heating stage at temperatures above Tc. It is important to mention that the logical function is valid for all the samples studied in this work, and the only difference between them are the S_{REL} values which also depend on the length of the organic chain.

3. EXPERIMENTAL SECTION

3.1 Materials

Europium(III) chloride hexahydrate ($EuCl_3$ $(H_2O)_6$, 99.9%), Terbium(III) chloride hexahydrate ($TbCl_3$ $(H_2O)_6$, 99.9%), 2,6-Pyridinedicarboxylic acid (DPA, 99%), *tert*-butyl acetoacetate, (3-Aminopropyl) triethoxysilane (APTES), Diethyleneglycol (DEG),

Poly(ethylene glycols) (PEG200, Mn: 200 PEG400, Mn: 400 Da; PEG600, Mn: 600 Da; PEG1000, Mn: 1000 Da, PEG300, Mn: 3000 Da), N,N-dimethylaniline (DMA) and acryloyl chloride (97%) were purchased from Aldrich and used as received.

3.2 Synthesis of polymers

The synthesis of the β-ketoester polyethylene glycol acrylates (acacPEGA [2]) was carried out in a two-step process according to the synthetic route shown in scheme S1. In a first step the β-ketoester group was introduced by a transesterification reaction between tert-butyl acetoacetate and commercial polyethylenglycol diols. Pure mono β-ketoester polyethylene glycols (acacPEG) were obtained by an extraction/fractionation method. The final polymers were obtained by reaction of the terminal hydroxyl groups of the pure mono acacPEG derivatives [1] with acryloyl chloride in the presence of DMA as HCl scavenger. The presence of the functional groups was confirmed by FTIR spectroscopy. (S3a-b).

3.2.1 Synthesis of Polyethylene glycols acetoacetate derivatives [1-6a]

A mixture of PEG (50 mmol) and tert-butyl acetoacetate (10.4 mL, 62.5 mmol) was heated at 60ºC and stirred for 60-72 hours. Distilled water was added to the reaction mixture (3 mL per gram of starting amount of PEG) and the aqueous solution was extracted twice with diethyl ether. The organic phase was discarded and the aqueous phase was fractional extracted with a mixture of dichlomethane/n-hexane (3:1), each fraction was dried over magnesium sulfate, concentrated under vacuum and purity analyzed by mass spectroscopy. Fractions with a small percent of di-β-ketoester or diols derivatives were combined and purified again following the same solvent extraction procedure. The absence of diol or di-β-ketoester impurities was confirmed by ESI-MS [6a] and MALDI-TOF MS [1-5a]. **Figure S2** shows the mass spectrum of pure acacPEG [1-6a] and their corresponding acacPEGA [1-6b].

3.2.2 Synthesis of acetoacetyl polyethylenglycol acrylate (acacPEGA)

To a solution of the corresponding acacPEG [1] (5mmol) in anhydrous THF (25 mL) cooled in an ice-water bath and DMA (0.7 mL, 5.5 mmol) and acryloyl chloride (0.46 mL, 5.5 mmol) were added were dropwise were added consecutively under argon atmosphere. The mixture was stirred for 48 hours at room temperature. Solvent was removed under pressure in a rotatory evaporator after adding a few grains of radical inhibitor BHT. The crude was dissolved in chloroform and the organic phase was washed with hydrochloric acid 2N, distilled water and brine, dried over magnesium sulphate and solvent evaporated under reduced pressure. Low molecular weight derivatives [3-6b]

were purified by dissolving in diethyl ether and precipitate in col n-hexane while derivates with higher molecular weight [1-2b] were dissolved in dichloromethane and precipitated in cold ether. Purity were checked by MS (See Figure S2) and NMR spectroscopy (SI file). Molecular weight of the purified monomers were determined from the ^{1}H-NMR signals

The purity of the derivatives was checked after each step by ^{1}H-NMR and Maldi-toff or ESI mass spectroscopy. Monomodal distributions were observed for almost all the compounds, $[M + Na]^+$ ions of the mono β-ketoesters were clearly observed whereas no signal of the diol, di β-ketoesters or diacrylate derivatives (Figures S2a-f) except for the PEG200 derivatives. In this case a small fraction of the diketoester derivate (5%) was detected. The final compound was used without further purification as this byproduct cannot react with the activated surfaces. The presence of the functional groups was confirmed by FTIR spectroscopy. (S3a-b)

3.3 Production of Functionalized Si surfaces

The procedure to coat the silicon surfaces with the thermometric probes has been described in a previous report.[36]

Briefly, P-type monocrystalline Si wafers (Okmetic) were coated with a SiO_2 layer of 1083.0 ± 11.3 nm thickness by Plasma-Enhanced Chemical Vapor Deposition (PECVD) of TEOS (tetraethylorthosilicate) at 380ºC, and a pressure of 1000 mTorr.

The wafers were cut into 1×1 cm^2 pieces, and the surface was activated by ozone treatment in an UVO-cleaner Model 342 (Jelight Company Inc., USA) during 10 minutes. Then, they were coated with (3-aminopropyl)triethoxysilane (APTES) by vapor deposition in a desiccator in vacuum, at 80°C, during 3 hours. Then, the samples were washed with acetone, dried under nitrogen, and cured on an oven at 50−60 °C for 20 minutes.

PEG polymer chains were grafted by Michael reaction of acrylate terminal groups with surface amine groups in water at pH = 8.5, at 60 °C. Two series of samples were prepared, B and D, with Michael reaction times 24h and 48h, respectively.

Tb^{3+} and Eu^{3+} ions in a 3.23 molar ratio were attached by coordination to the acac polymer terminal groups at pH = 6.7 during 3 hours. Then, the lanthanide complexes were completed by addition of DPA and reaction overnight. The surfaces were then thoroughly washed with distilled water and dried under nitrogen.

Six samples in each series were prepared using acacPEGA polymers with different PEG chain length, namely: 3000 (Sample Z6(B and D)), 1000 (Sample Z5(B and D)), 600 (Sample Z4(B and D)), 400 (Sample Z3(B and D)), 200 (Sample Z2(B and D)), 100 (Sample Z1(B and D)).

3.4 Methods

3.4.1 Chemical characterization

The molecular structure and purity of all the polyethylene glycol derivatives was confirmed by Nuclear magnetic resonance (NMR), Mass spectroscopy (MS) and Infrared spectroscopy (IR). Proton (^{1}H) and carbon (^{13}C) NMR spectra were recorded at room temperature solvent in a BRUKER AV-400 spectrometer (400 MHz (^{1}H), 100 MHz (^{13}C)) using CDCl$_3$ as solvent. ^{1}H and ^{13}C chemical shifts (δ) are reported in ppm and are referenced to the solvent peak (CDCl$_3$: $\delta H = 7.26$ ppm, $\delta C = 77.00$ ppm), the coupling constants (J) are given in Hz. Signals were assigned by first-order analysis and the assignments were supported by two-dimensional ^{1}H-^{13}C HSQC experiments. Purity was checked by MALDI TOF mass spectroscopy using dithranol (DTH) as matrix and sodium trifluoroacetate (NaTFA) as cationization agent in a BrukerMicroFlex spectrometer. ESI-MS spectra for the diethylenglycol based derivatives were recorded on an Esquire 3000 plus instrument from Bruker Daltonics (S2a-f). FT-IR spectra were recorded in a Perkin Elmer Spectrum 100 FT-IR spectrometer equipped with a Universal ATR sampling accessory. The spectra were collected over the range 4000-380cm^{-1} and ATR correction (S3 a-b).

3.4.2 Surface characterization

AFM and FESEM. Atomic force microscopy (AFM) and field emission scanning electron microscopy (FESEM) were carried out, respectively, in a Ntegra Aura (NT-MDT) equipment and in a Carl Zeiss MERLIN™ microscope.

XPS. The X-ray photoelectron spectroscopy (XPS) analysis was carried out using a Kratos Axis Ultra spectrometer employing a monochromatic Al K$_\alpha$ (1486,6 eV)10 mA, 15 kV) X-ray source and a power of 150 W. All samples were introduced in the analysis chamber simultaneously and were analysed in the same experimental conditions. In order to avoid any induced effect in the chemistry of the samples, they were analysed as received without any previous etching. Differential surface charging was minimized using a charge neutralizer system (flood gun). Survey spectra were recorded using analyser pass energy of 160 eV and 1.0 eV energy step. High resolution spectra of C 1s, O 1s, N 1s, Si 2p, Eu 3d and Tb 3d regions were collected using pass energy of 20 eV 0.1

eV energy step. The spectra were analysed using CasaXPS® software. The background for all spectra was subtracted using a Shirley baseline. Due to the use of charge neutralizer, spectra need to be calibrated. Binding Energies (B.E.) were referenced to the C 1s (C-C) peak at 285.0 eV.

Photoluminescence and Temperature Control: The emission spectra were recorded with a modular double grating excitation spectrofluorimeter with a TRIAX 320 emission monochromator (Fluorolog-3, Horiba Scientific) coupled to a R928 Hamamatsu photomultiplier, using a front face configuration. A 450 W Xe arc lamp was used as the excitation source. Both recorded emission and excitation spectra were corrected with the spectrofluorimeter optical spectral response and the spectral distribution of the lamp intensity using a photodiode reference detector respectively. On the other hand, the temperature was controlled using an IES-RD31 controller and a Kapton thermofoil heater from Minco mounted on a copper holder and monitored using a thermo-couple thermometer Barnant 100 (model 600-2820) with an accuracy of 0.1 K, accordingly to the manufacturer. The temperature ramp in the heating–cooling cycles is about 0.25 K min^{-1}.

References

1   Madhuprasad, M. P. Bhat, H. Y. Jung, D. Losic and M. D. Kurkuri, *Chem. - A Eur. J.*, 2016, **22**, 6148–6178.
2   M. a Reed and J. M. Tour, *Sci. Am.*, 2000, **18**, 53–58.
3   J. M. Tour, *Acc. Chem. Res.*, 2000, **33**, 791–804.
4   L. Sun, Y. A. Diaz-Fernandez, T. A. Gschneidtner, F. Westerlund, S. Lara-Avila and K. Moth-Poulsen, *Chem. Soc. Rev.*, 2014, **43**, 7378–7411.
5   J. M. Tour, *Chem. Rev.*, 1996, **96**, 537−553.
6   P. A. De Silva, N. H. Q. Gunaratne and C. P. McCoy, *Nature*, 1993, **364**, 42–44.
7   A. Prasanna De Silva, *Chem. - An Asian J.*, 2011, **6**, 750–756.
8   A. P. De Silva, *J. Phys. Chem. Lett.*, 2011, **2**, 2865–2871.
9   A. P. De Silva, C. M. Dobbin, T. P. Vance and B. Wannalerse, *Chem. Commun.*, 2009, 1386–1388.
10   A. P. De Silva, T. P. Vance, M. E. S. West and G. D. Wright, *Org. Biomol. Chem.*, 2008, **6**, 2468–2481.
11   A. P. de Silva and S. Uchiyama, *Nat. Nanotechnol.*, 2007, **2**, 399–410.
12   H. Komatsu, S. Matsumoto, S. ichi Tamaru, K. Kaneko, M. Ikeda and I. Hamachi, *J. Am. Chem. Soc.*, 2009, **131**, 5580–5585.
13   M. Moshe, J. Elbaz and I. Willner, *Nano Lett.*, 2009, **9**, 1196–1200.
14   F. Pu, C. Wang, D. Hu, Z. Huang, J. Ren, S. Wang and X. Qu, *Mol. Biosyst.*, 2010, **6**, 1928–1932.
15   F. Pu, J. Ren, X. Yang and X. Qu, *Chem. - A Eur. J.*, 2011, **17**, 9590–9594.
16   P. L. Gentili, *J. Phys. Chem. A*, 2008, **112**, 11992–11997.
17   F. Pu, E. Ju, J. Ren and X. Qu, *Adv. Mater.*, 2014, **26**, 1111–1117.

18   R. Arabahmadi, *Talanta*, 2019, **194**, 119–126.

19   S. Zeng, S. J. Li, X. J. Sun, M. Q. Li, Y. Q. Ma, Z. Y. Xing and J. L. Li, *Spectrochim. Acta - Part A Mol. Biomol. Spectrosc.*, 2018, **205**, 276–286.

20   Y.-W. Wang, S.-B. Liu, Y.-L. Yang, P.-Z. Wang, A.-J. Zhang and Y. Peng, *ACS Appl. Mater. Interfaces*, 2015, **7**, 4415–4422.

21   M. L. Liu, B. Bin Chen, J. H. He, C. M. Li, Y. F. Li and C. Z. Huang, *Talanta*, 2019, **191**, 443–448.

22   Z. H. Chen, X. Y. Han, L. X. Deng, Z. Y. Lin, F. Y. Mu, S. Zhang, G. Shi and M. Zhang, *Talanta*, 2019, **191**, 235–240.

23   S. Maji, S. Kumar and K. Sankaran, *Spectrochim. Acta - Part A Mol. Biomol. Spectrosc.*, 2015, **135**, 405–409.

24   M. S. Tremblay, Q. Zhu, A. A. Martí, J. Dyer, M. Halim, S. Jockusch, N. J. Turro and D. Sames, *Org. Lett.*, 2006, **8**, 2723–2726.

25   T. Gunnlaugsson and J. P. Leonard, *Chem. Commun.*, 2005, 3114–3131.

26   L. K. Truman, S. J. Bradberry, S. Comby, O. Kotova and T. Gunnlaugsson, *ChemPhysChem*, 2017, **18**, 1746–1751.

27   J. Yu, D. Parker, R. Pal, R. A. Poole and M. J. Cann, *J. Am. Chem. Soc.*, 2006, **128**, 2294–2299.

28   T. Gunnlaugsson, D. a. Mac Dónail and D. Parker, *Chem. Commun.*, 2000, 93–94.

29   Z. Dou, J. Yu, Y. Cui, Y. Yang, Z. Wang, D. Yang and G. Qian, *J. Am. Chem. Soc.*, 2014, **136**, 5527–5530.

30   J. Rocha, C. D. S. Brites and L. D. Carlos, *Chem. - A Eur. J.*, 2016, **22**, 14782–14795.

31   H. Xu, C. S. Cao and B. Zhao, *Chem. Commun.*, 2015, **51**, 10280–10283.

32   J. N. Hao and B. Yan, *Chem. Commun.*, 2015, **51**, 7737–7740.

33   S. Y. Zhang, W. Shi, P. Cheng and M. J. Zaworotko, *J. Am. Chem. Soc.*, 2015, **137**, 12203–12206.

34   H. Y. Li, Y. L. Wei, X. Y. Dong, S. Q. Zang and T. C. W. Mak, *Chem. Mater.*, 2015, **27**, 1327–1331.

35   X. Y. Xu and B. Yan, *Adv. Funct. Mater.*, 2017, **27**, 1–11.

36   M. Rodrigues, R. Piñol, G. Antorrena, C. D. S. Brites, N. J. O. Silva, J. L. Murillo, R. Cases, I. Díez, F. Palacio, N. Torras, J. A. Plaza, L. Pérez-García, L. D. Carlos and A. Millán, *Adv. Funct. Mater.*, 2016, **26**, 200–209.

37   T. L. Miller and S. I. Senkfor, *Anal. Chem.*, 1982, **54**, 2022–2025.

38   C. D. S. Brites, P. P. Lima and L. D. Carlos, *J. Lumin.*, 2016, **169**, 497–502.

39   M. Latva, H. Takalo, V.-M. Mukkala, C. Matachescu, J. C. Rodriguez-Ubis and J. Kankare, *J. lu*, 1997, **75**, 149–169.

40   C. D. S. Brites, P. P. Lima, N. J. O. Silva, A. Millán, V. S. Amaral, F. Palacio and L. D. Carlos, *Adv. Mater.*, 2010, **22**, 4499–4504.

41   L. D. Carlos, V. De Zea Bermudez, V. S. Amaral, S. C. Nunes, N. J. O. Silva, R. A. Sá Ferreira, J. Rocha, C. V. Santilli and D. Ostrovskii, *Adv. Mater.*, 2007, **19**, 341–348.

42   R. Piñol, C. D. S. Brites, R. Bustamante, A. Martínez, N. J. O. Silva, J. L. Murillo, R. Cases, J. Carrey, C. Estepa, C. Sosa, F. Palacio, L. D. Carlos and A. Millán, *ACS Nano*, 2015, **9**, 3134–3142.

43   C. D. S. Brites, P. P. Lima, N. J. O. Silva, A. Millán, V. S. Amaral, F. Palacio and L. D. Carlos, *Front. Chem.*, 2013, **1**, 1–6.

44   P. Goldner, O. Guillot-Nöel and P. Higel, *Opt. Mater. (Amst).*, 2004, **26**, 281–286.

45   M. P. Hehlen, H. U. Güdel, Q. Shu, J. Rai, S. Rai and S. C. Rand, *Phys. Rev. Lett.*, 1994, **73**, 1103–1106.

46   A. Ródenas, D. Jaque, J. García Solé, A. Speghini, M. Bettinelli and E. Cavalli, *Opt. Mater. (Amst).*, 2006, **28**, 1280–1283.

47   D. Ananias, F. A. A. Paz, D. S. Yufit, L. D. Carlos and J. Rocha, *J. Am. Chem. Soc.*, 2015, **137**, 3051–3058.

48   C. Xia, C. Yu, M. Cao, J. Xia, D. Jiang, G. Zhou, D. Zhang and H. Li, *Ceram. Int.*, , DOI:10.1016/j.ceramint.2018.08.140.

49   Y. Cui, W. Zou, R. Song, J. Yu, W. Zhang, Y. Yang and G. Qian, *Chem. Commun.*, 2014, **50**, 719–721.

50   C. D. S. Brites, P. P. Lima, N. J. O. Silva, A. Millán, V. S. Amaral, F. Palacio and L. D. Carlos, *J. Lumin.*, 2013, **133**, 230–232.

51   A. M. Kaczmarek, D. Esquivel, B. Laforce, L. Vincze, P. Van Der Voort, F. J. Romero-Salguero and R. Van Deun, *Luminescence*, 2018, **33**, 567–573.

52   H. Wang, D. Zhao, Y. Cui, Y. Yang and G. Qian, *J. Solid State Chem.*, 2017, **246**, 341–345.

53   S. Zheng, W. Chen, D. Tan, J. Zhou, Q. Guo, W. Jiang, C. Xu, X. Liu and J. Qiu, *Nanoscale*, 2014, **6**, 5675–5679.

54   S. N. Zhao, L. J. Li, X. Z. Song, M. Zhu, Z. M. Hao, X. Meng, L. L. Wu, J. Feng, S. Y. Song, C. Wang and H. J. Zhang, *Adv. Funct. Mater.*, 2015, **25**, 1463–1469.

55   Y. H. Han, C. Bin Tian, Q. H. Li and S. W. Du, *J. Mater. Chem. C*, 2014, **2**, 8065–8070.
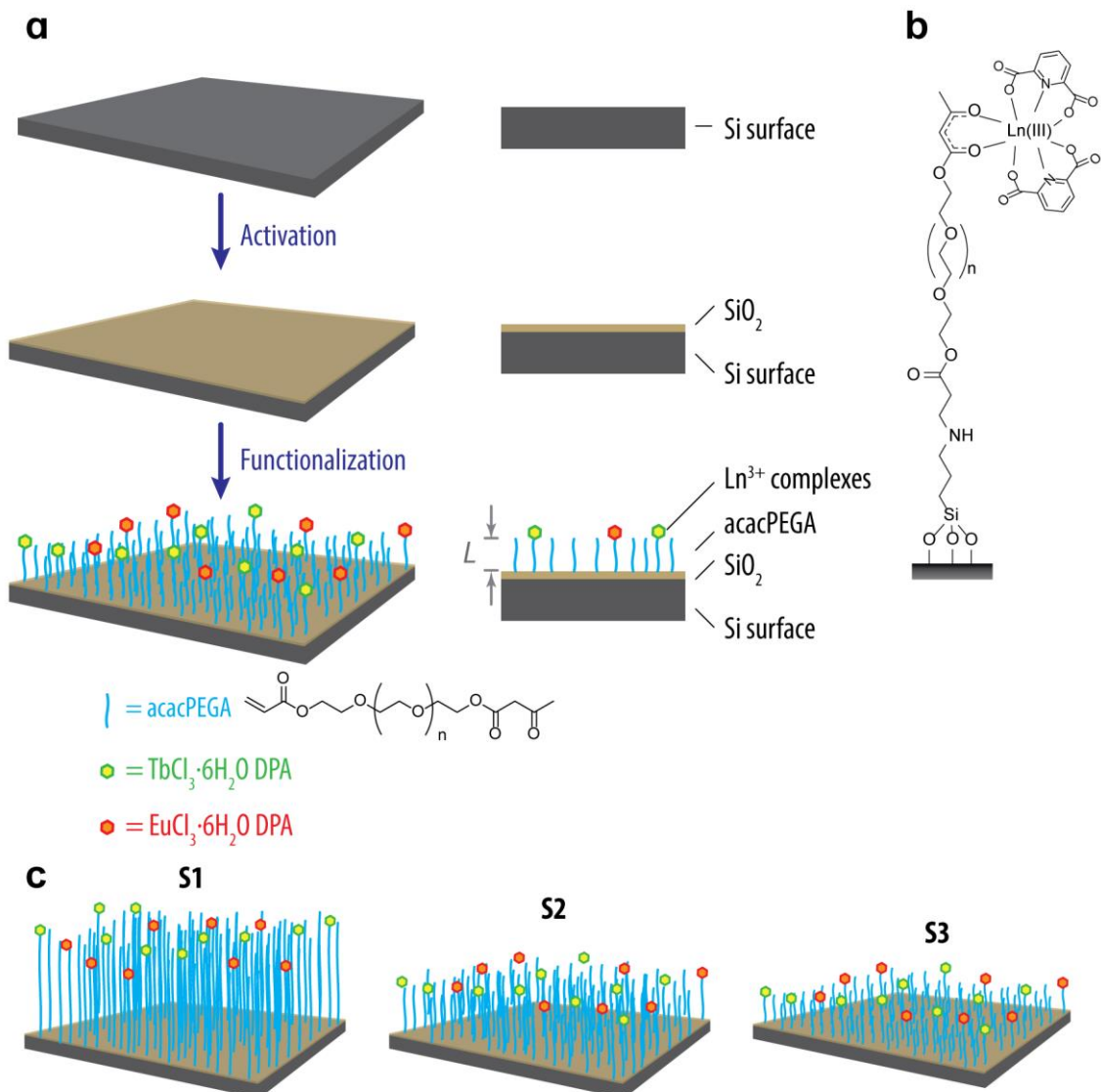
Figure 1. (a) Schematic diagram of Si surface functionalization with thermometric SAM showing the activation and functionalization steps. **(b)** Structural formula of the Si surface functionalization with thermometric SAM **(c)** Schematic representation of samples S1, S2 and S3.
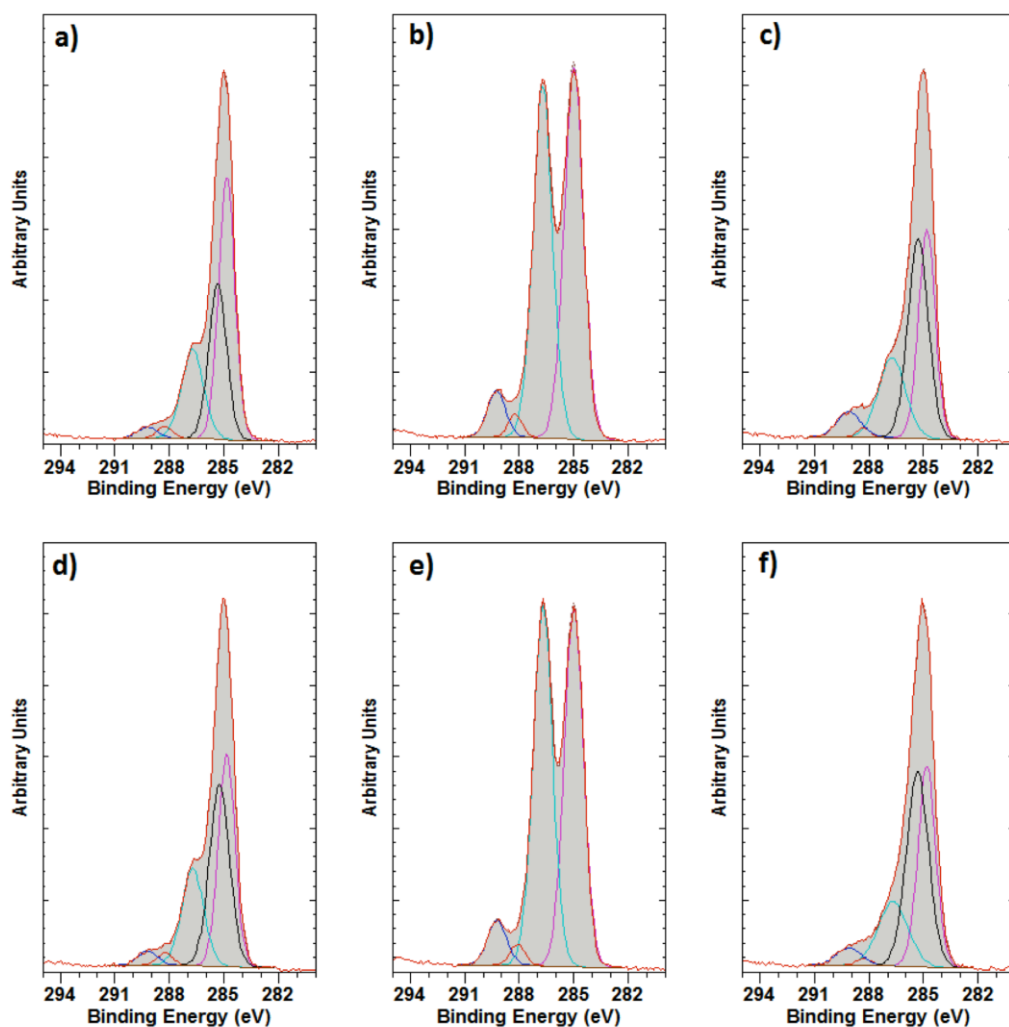
Figure 2. XPS spectra of the C 1s region in samples Z1A (a), Z3A (b), Z6A (c),Z1C (d), Z3C (e) and Z6C (f). Expected oxidation states for Carbon in acacPEGA are identified: C-C (pink & black), C-O (cyan), O-C-O/C=O (red) and O-C=O (blue).

Remarkable differences are found in C-O signal depending on the length of acacPEGA chain, (Z1A/Z1D longest, Z3A/Z3D middle lenght and Z6A/Z6D shortest). Series B and D show the same behavior.
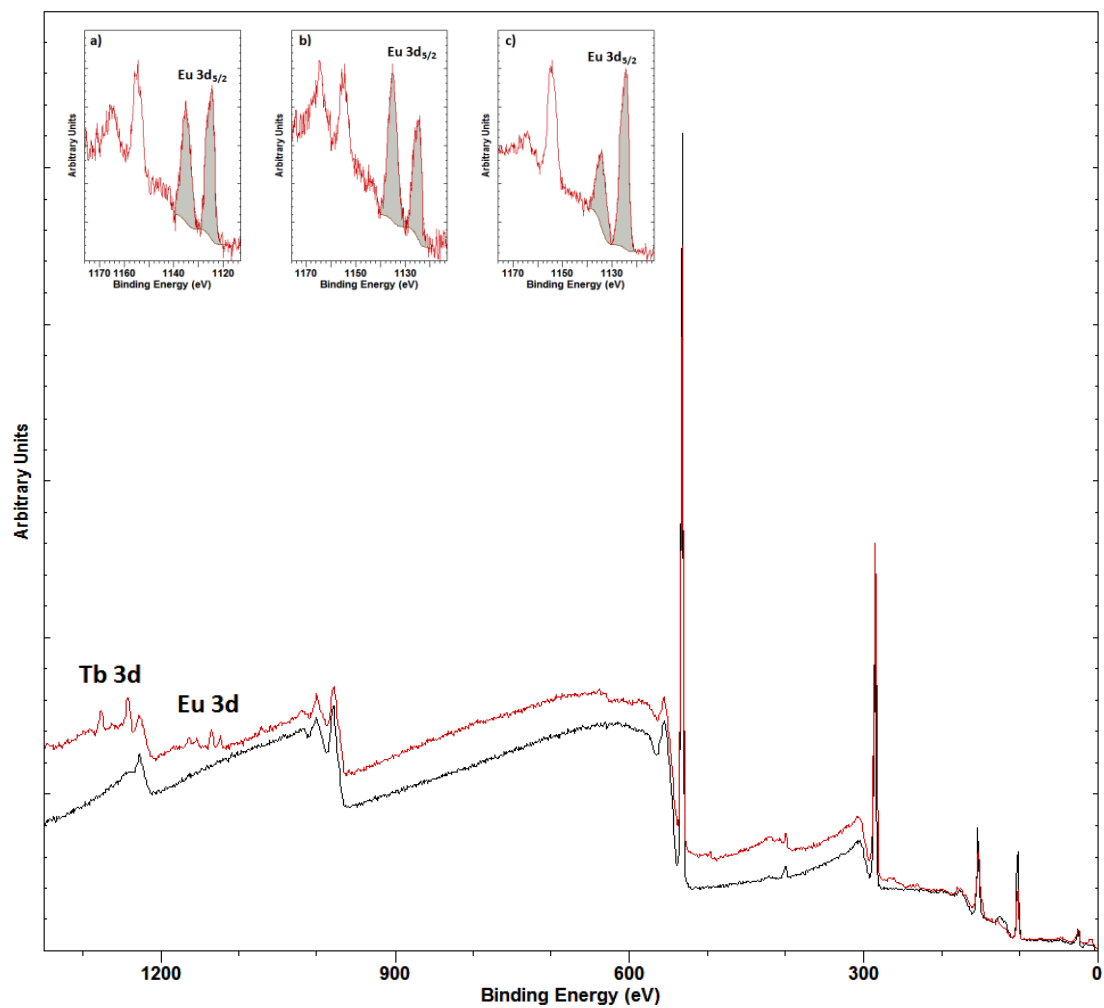
Figure 3. XPS wide spectra for sample Z3A (black) and Z3B (red), before and after anchoring the Ln^{3+} complexes respectively. The insert shows the evolution of Eu 3d core level with the length of the acacPEGA organic chain Z1B (a), Z2B (b) and Z3B (c).
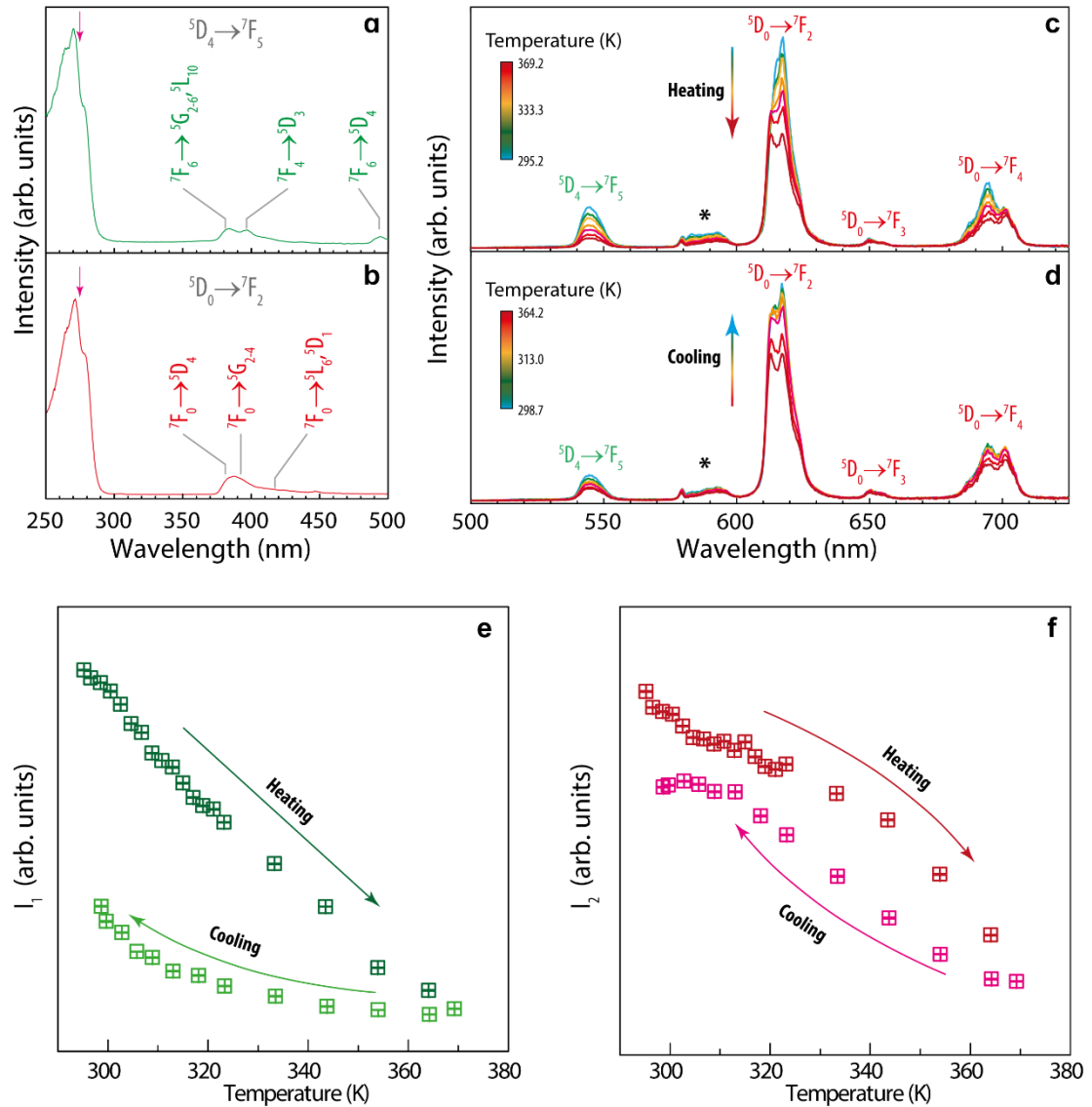
Figure 4. a) Excitation spectra of the self-assembled monolayer (SAM) of polymer functionalized Si surface doped with Tb^{3+}-Eu^{3+} with the shortest organic chain (Z6D1) at 295 K, monitoring the $^5D_4 \rightarrow {}^7F_5$ (Tb^{3+}) and $^5D_0 \rightarrow {}^7F_2$ (Eu^{3+}) transitions, respectively. b) Emission spectra in a single heating-cooling cycle from 295 K up to 369 K exciting at 271.5 nm. The transitions assigned the Tb^{3+} and Eu^{3+} ions are presented in green and orange colours respectively, the asterisk marks the spectral region where an overlap between the Tb^{3+} transition $^5D_4 \rightarrow {}^7F_4$ and Eu^{3+} transitions $^5D_0 \rightarrow {}^7F_{0,1}$ is observed. c) Integrated intensity area of the $^5D_4 \rightarrow {}^7F_4$ (Tb^{3+}) (top) and $^5D_0 \rightarrow {}^7F_2$ (Eu^{3+}) (bottom)

transitions in a single heating–cooling cycle between 295 K up to 369 K, obtained from the emission spectra under 271.5 nm excitation.

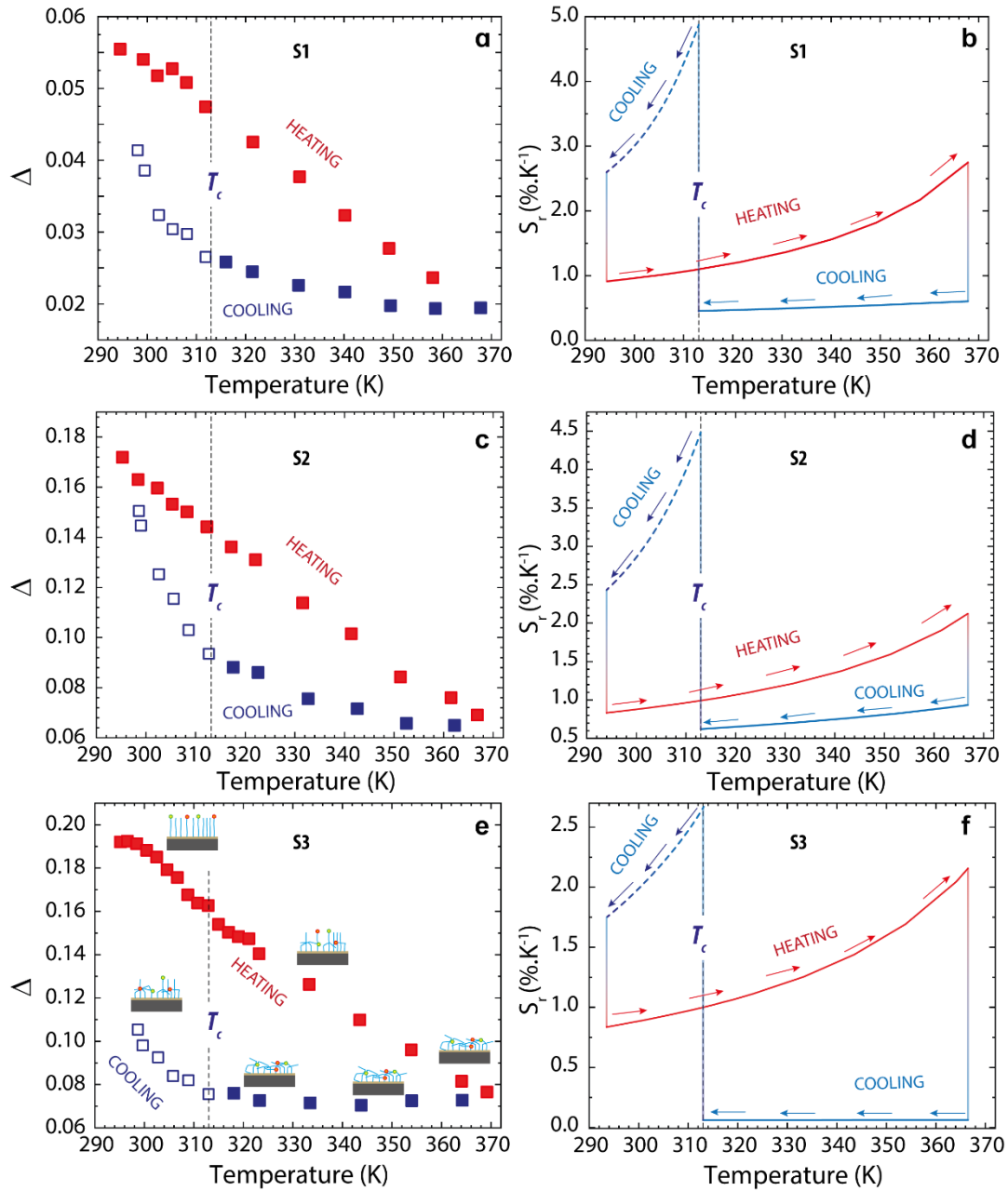**Figure 5.** Temperature evolution of the thermometric parameter Δ (defined as I_1/I_2, where I_1 and I_2 are the integrated intensity areas of the emission bands associated to the $^5D_4 \rightarrow\ ^7F_5$ (Tb^{3+}) and $^5D_0 \rightarrow\ ^7F_2$ (Eu^{3+}) transitions, respectively from 295 K up to 369 K in a single heating–cooling cycle (symbols, blue open symbols represent regime 2) for the samples with the (a) longest, (c) organic chain middle one and (e) shortest one (Z1D1, Z3D1, Z6D1, respectively). The relative sensitivities, S_{REL} are also given for the samples with the longest organic chain length (Z1D1) to the shortest one (Z6D1).
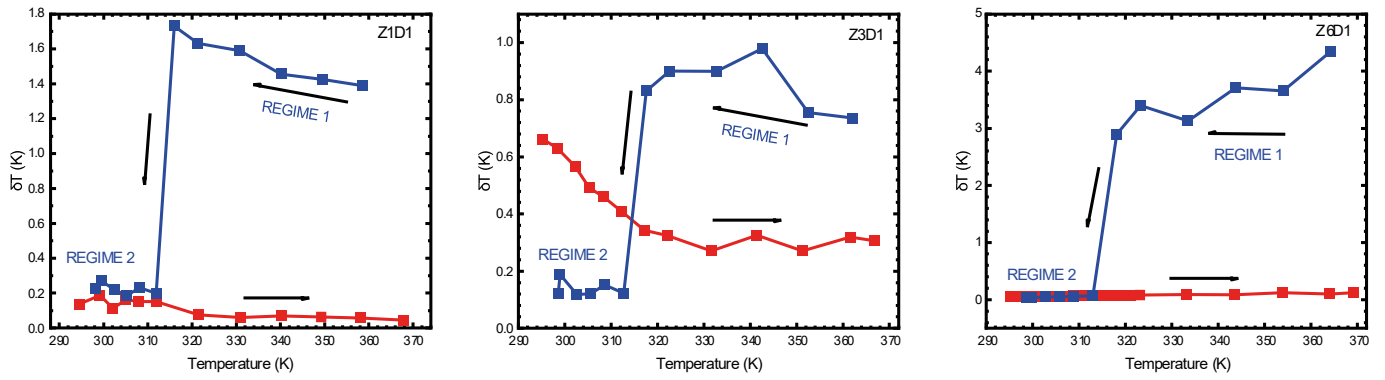
Figure 5. Temperature uncertainty (δT) as a function of the temperature of the samples.

Table 1 Excitation wavelength (λ_{EXC}), transitions involved in the temperature calibration procedure, temperature range (ΔT), maximum relative sensitivity (S_M), and temperature for which it happens (T_M), of different Ln^{3+}-based thermometers involving the $^5D_4 \rightarrow {}^7F_5$ and $^5D_0 \rightarrow {}^7F_2$ transitions of Tb^{3+} and Eu^{3+} respectively.

Optical sensor	λ_{EXC} (nm)	ΔT (K)	S_M (% K^{-1})	T_M (K)	Ref.
S1 (former Z1D1)	271.5	295-369	2.84	369	This work
S2 (former Z3D1)	271.5	295-369	2.73	369	This work
S3 (former Z6D1)	271.5	295-369	2.24	369	This work
Na[(Gd$_{0.8}$Eu$_{0.1}$Tb$_{0.1}$)SiO$_4$]	483.5	12-450	2.0	20	[47]
MOF-5: Eu^{3+}-Tb^{3+}	325	303-473	1.8	473	[48]
Tb$_{0.957}$Eu$_{0.043}$cpda	335	40-300	1.77	250	[49]
γ-F$_2$O$_3$@TEOS/APTES: Eu^{3+}-Tb^{3+} (NP5-1.4)	315	10-325	1.5	315	[50]
Eu^{3+}-Tb^{3+} functionalized SAM	280	296-338	1.43	323	[36]
dppz-vSilica@Eu, Tb	295	10-360	1.32	260	[51]
MOF: Tb^{3+}-Eu^{3+}	296	313-473	0.52	313	[52]
NaGdF$_4$:Yb/Tm@Tb/Eu	980	125–300	0.49	300	[53]
Na[(Gd$_{0.8}$Eu$_{0.1}$Tb$_{0.1}$)SiO$_4$]	483.5	10-425	0.3	300	[47]
Tb$_{0.7}$Eu$_{0.3}$L	322	40-300	0.17	300	[54]
{Tb$_{0.3}$Eu$_{0.7}$(D-cam)(Himdc)$_2$·(H$_2$O)$_2$}$_3$ *	277	100-450	0.11	450	[55]

* D-H$_2$cam = D-camphoric acid, H$_3$imdc = 4,5-imidazole dicarboxylic acid (ligands)

Table 2. Truth table for the logic gates on heating (295−369 K) (cooling from 369 to 295 K)

Entry	Input-1 λ_{Exc} (370 nm)	Input-2 (T>T$_c$)	Input-3 ΔT (Heating)	Output-1 S_{REL}^{A} (Heating Regime)	Output-2 S_{REL}^{B} (Cooling Regime 1)	Output-3 S_{REL}^{C} (Cooling Regime 2)
1	0	0	0	0	0	0
2	0	0	1	0	0	0
3	0	1	0	0	0	0
4	0	1	1	0	0	0
5	1	0	0	0	0	1
6	1	0	1	1	0	0
7	1	1	0	0	1	0
8	1	1	1	1	0	0